Published in final edited form as:
*J Control Release*. 2007 December 4; 124(1-2): 11–19.

# Modeling Doxorubicin Transport to Improve Intratumoral Drug Delivery to RF Ablated Tumors

**Brent D. Weinberg**[1,3], **Ravi B. Patel**[1], **Agata A. Exner**[2], **Gerald M. Saidel**[1], and **Jinming Gao**[3]

1 *Department of Biomedical Engineering, Case Western Reserve University, Cleveland, OH 44106*

2 *Department of Radiology, Case Western Reserve University, Cleveland, OH 44106*

3 *Simmons Comprehensive Cancer Center, University of Texas Southwestern Medical Center, Dallas, TX 75390*

## Abstract

A mathematical model of drug transport provides an ideal strategy to optimize intratumoral drug delivery implants to supplement radiofrequency (RF) ablation for tumor treatment. To simulate doxorubicin transport in non-ablated and ablated liver tumors, a one-dimensional, cylindrically symmetric transport model was generated using a finite element method (FEM). Parameters of this model, the diffusion ($D$) and elimination ($\gamma$) coefficients for doxorubicin, were estimated using drug distributions measured 4 and 8 days after placing biodegradable implants in non-ablated and ablated rabbit VX2 liver carcinomas. In non-ablated tumor, values of diffusion and elimination parameters were 25% and 94% lower than normal liver tissue, respectively. In ablated tumor, diffusion near the ablation center was 75% higher than non-ablated tumor but decreased to the non-ablated tumor value at the ablation periphery. Drug elimination in ablated tumor was zero for the first four days, but by day 8 returned to 98% of the value for non-ablated tumor. Three-dimensional (3-D) simulations of drug delivery from implants with and without RF thermal ablation underscore the benefit of using RF ablation to facilitate local drug distribution. This study demonstrates the use of computational modeling and optimal parameter estimation to predict local drug pharmacokinetics from intratumoral implants after ablation.

### Keywords

biodegradable implant; local chemotherapy; radiofrequency ablation; mathematical modeling; VX2 tumor

## Introduction

Treatment of unresectable tumors has been supplemented in recent years by the development of minimally invasive interventions, such as laser [1], microwave [2], and radiofrequency (RF) ablation [3]. RF ablation in particular has shown improved efficacy in the treatment of hepatocellular carcinoma (HCC) [4], where approximately 80% of tumors cannot be surgically

Correspondence and reprint requests should be addressed to: Jinming Gao, Simmons Comprehensive Cancer Center, University of Texas Southwestern Medical Center, 6001 Forrest Park, Rm ND2.210, Dallas, TX 75390, Phone: 214-645-6370, Fax: 214-645-6347, E-mail: jinming.gao@utsouthwestern.edu.

removed [5]. However, despite its success, RF ablation is restricted by limited ablation sizes that can be created with a single treatment as well as the risk of tumor recurrence around the boundary [6,7]. Biodegradable polymer implants, termed polymer millirods, have been designed to deliver chemotherapeutic agents to the RF treated region to kill residual tumor cells and prevent tumor recurrence [8–10]. These implants have been studied systematically in non-ablated and ablated liver tissues [11,12], and initial studies using doxorubicin-containing implants to treat tumors have indicated their potential benefit [13,14]. Up to now, the major challenge in effectively treating tumors with polymer millirods has been the limited drug penetration distance into the surrounding tissue. Although several changes to implant design have already been described [9,15], how these changes would affect local drug delivery efficiency and anti-tumor efficacy is not obvious.

A strategic method for improving implant therapy is to use a mathematical model to establish a mechanistic understanding of drug transport processes and how they affect drug pharmacokinetics and delivery efficiency [16–19]. Using a mathematical model to aid in polymer millirod design has several advantages over empirical experimental testing. First, measurement of doxorubicin transport parameters in tumor tissue provides insight into differences between tissue types and cellular changes that result from RF ablation. This information allows for a better understanding of why a particular treatment may be effective and allows for better treatment design. Second, model simulation can be used to test a wide variety of treatment conditions while minimizing the number of animal subjects. Different drug release profiles, implant locations, or number of implants can be modeled, and only the best available treatments need to be tested in animals. Third, drug distributions can be predicted in larger tumors that are a better approximation of clinical cases. Tumors in rat and rabbit models typically range from 0.5 – 2.0 cm in diameter, but human tumors are often 5.0 cm or larger when first treated [20]. By simulating treatments in these larger tumors, problems in treatment scale-up can be anticipated and addressed. These advantages make a distinct argument for using mathematical modeling to improve post-ablation drug delivery.

Other studies have established a precedent for using modeling to design local drug delivery systems. Strasser et al. estimated a coefficient of elimination and diffusion to explain differences in transport of several different drugs away from polymers implanted in the brain [21]. Wang et al. used model simulation of BCNU delivery to brain tumors with implants to establish the value of combination treatment using surgical debulking and intratumoral ethylene-vinyl acetate implants [22]. Other studies have delved into the specific factors influencing drug transport surrounding implants in the brain [23] and increased the complexity of model simulations [24]. In the area of convection enhanced delivery (CED), in which a microcatheter is used to instill drugs into the center of a brain tumor, computational modeling has been used to optimize treatment parameters, such as infusion rate and pressure, to maximize the area treated by drug infusion [25–27]. Transport modeling has also been used to describe how modification of the tissue properties of a tumor, such as using a drug pretreatment to increase the diffusion rate, can affect drug penetration into tumors [28,29]. Valuable conclusions drawn from these works emphasize the value of modeling to optimize drug delivery to solid tumors, where drug distribution is often limited by poor perfusion and limited diffusion distances.

A model to describe local drug transport in the tissue surrounding polymer millirods has already been introduced in our previous publications. Qian et al. introduced a mass transport model that described the radially outward transport of doxorubicin (DOX) away from the polymer millirod surface using diffusion and elimination terms [9]. This model could be analytically solved to determine drug release rates necessary to create a desired drug concentration at the boundary of an ablated liver region. In a subsequent application of this model, doxorubicin diffusion and elimination parameters in non-ablated and ablated liver tissue were estimated,

providing initial insights about how ablation influences local drug transport by dramatically decreasing drug elimination [10]. Together, these studies demonstrated the feasibility of using a model to predict local drug delivery from polymer millirods in non-ablated and ablated liver. However, the applicability of this model to drug transport in tumors has not been investigated.

The goal of this paper is to extend the previously developed doxorubicin transport model to describe transport in non-ablated and ablated liver tumors. To accomplish this goal, two different implementations of a mass transport model incorporating doxorubicin diffusion and elimination in tumors were developed. First, a one-dimensional (1-D), cylindrically symmetric transport model was used to simulate intratumoral doxorubicin release from polymer millirods. Parameters of this doxorubicin transport model were estimated using nonlinear least-squares estimation to minimize the error between the model output and experimentally measured DOX concentration distributions. Second, a three-dimensional (3-D) implementation of the drug transport model was used to simulate treatment of larger tumors with RF ablation and polymer millirods. This implementation was used to demonstrate how this model can be effective in predicting doxorubicin distributions in different tumor treatment scenarios. Results from this paper provide essential information about doxorubicin transport and elimination in tumors and will ultimately be used to improve future intratumoral treatment with polymer millirods.

## Experimental Methods

### Implant fabrication

Implants were produced by a compression-heat molding procedure [30]. Poly(D,L-lactide-co-glycolide) (PLGA; 1:1 lactide/glycolide; inherent viscosity 0.65 dL/g) was obtained from Birmingham Polymers (Birmingham, AL) and was made into microspheres using a single emulsion method. Doxorubicin HCl (DOX) (2 mg/mL) in saline (9 mg/mL) was acquired from Bedford Laboratories (Bedford, OH) and desalted before use. A mixture of 65% PLGA microspheres, 13.5% DOX, and 21.5% NaCl (w/w) was mixed with a mortar and pestle, packed into a Teflon tube (1.6 mm outside diameter), and compressed with steel plungers (1.6 mm inside diameter) at 90° C for 2 hours. Final implants were cylindrical with an approximate diameter of 1.5 mm and length of 8.0 mm.

### Non-ablated tumor treatment

All animal studies followed the guidelines of and were approved by the IACUC at Case Western Reserve University. Treatment of liver tumors in rabbits using doxorubicin-containing PLGA implants was reported in a previous publication [13]. Adult male New Zealand White rabbits (n = 14; Covance, Princeton, NJ) weighing 2.8–3.2 kg were used for all *in vivo* studies. VX2 liver carcinomas were generated in rabbit livers by surgically implanting a small piece (1 $mm^3$) of frozen tumor tissue in the rabbit liver. The tumors were grown in the liver for 12 days until they reached an approximate diameter of 8 mm. Then, the abdomen was surgically opened and a control or doxorubicin-containing implant was inserted into the center of the tumor and secured with a suture. The rabbits were euthanized 4 or 8 days after the onset of treatment, and the tumors were removed.

### Ablated tumor treatment

Combined treatment of liver tumors in rabbits with RF ablation followed by doxorubicin-containing polymer implants was also reported in a previous publication [14]. VX2 carcinomas were implanted as above but were allowed to grow for 18 days until they reached an approximate diameter of 11 mm. A 17-gauge ablation probe with a 1-cm exposed tip (Radionics, Burlington, MA) was placed into the center of the tumor. The tissue in contact with the tip was heated to 80°C for 2 min, which created a coagulated region of approximately 8 mm in diameter. After ablation, a control or doxorubicin-containing millirod was placed into

the electrode tract and secured with a suture. The rabbits were euthanized 4 or 8 days after the onset of treatment, and the tumors were removed.

### Tumor assessment

Tumors removed from the surrounding liver tissue were sliced in half perpendicular to the major axis of the implant. Half of the tumor was fixed in formalin solution and the other half was frozen at −20°C. The fixed tissue was embedded in paraffin, sliced, and stained with hematoxylin and eosin (H&E) or Masson's trichrome (MTC). Liver sections 100 μm thick were sliced from the frozen half of the tumor using cryostat microtome (Microm 505E) and then scanned with a fluorescent imager (Molecular Dynamics Fluorimager SI). For ablated tissue sections, the ablation background was adjusted for using a background subtraction algorithm [14]. Then, tumor net fluorescence intensity (NFI) was converted to doxorubicin concentration using a previously established calibration curve, $NFI = 194 \cdot [DOX]^{0.67}$, where [DOX] is the doxorubicin concentration in μg/g [13]. Radial drug distribution profiles as a function of distance from the implant center were determined by averaging four evenly spaced samples from the fluorescence image.

## Development of Drug Transport Model

### Drug transport model

Doxorubicin transport into tumor tissue from an implant device was analyzed by a dynamic mass balance transport model incorporating diffusion and elimination [10],

$$\frac{\partial C}{\partial t} = D\nabla^2 C - \gamma C \tag{1}$$

where $D$ and $\gamma$ represent apparent diffusion and elimination coefficients, respectively [10]. Drug elimination resulted from both perfusion and metabolism and was approximated as first order.

### Boundary and initial conditions

The boundary conditions were chosen to approximate experimental measurements. At the inner implant boundary,

$$r = R_{IB} : C = f(t) \tag{2}$$

where $f(t)$ is the time dependent concentration that was measured experimentally. At the outer normal tissue boundary,

$$r = R_{OB} : C = 0 \tag{3}$$

where $R_{OB}$ is the maximum extent of normal liver tissue included in the model. The concentration at this boundary was assumed to go to zero because of the elimination process. Initially, the tissue drug concentration was zero,

$$t = 0 : C = 0 \tag{4}$$

because there was no doxorubicin present in the tissue before the implants were placed. Drug flux and concentration were assumed continuous at all interior boundaries.

### One-dimensional (1-D) simulation method

Doxorubicin diffusion and elimination parameters were estimated for non-ablated and ablated tumor by implementing a 1-D, cylindrically symmetric simulation. For spherical tumors with a single cylindrical implant placed in the center, the dominant transport process occurs in the radial (*r*) direction, which can be described by a one-dimensional (1-D) model of the drug concentration distribution with time *C(r,t)*,

$$\frac{\partial C}{\partial t} = \frac{D}{r}\frac{\partial}{\partial r}\left(r\frac{\partial C}{\partial r}\right) - \gamma C \tag{5}$$

In both non-ablated and ablated tissue models, a single polymer implant (r = 0.8 mm) was located at the tumor center. In experimental studies of non-ablated VX2 liver tumors treated with a doxorubicin implant, the tumor radius began as 4 mm but decreased to 2.4 and 2.1 mm after 4 and 8 days, respectively, responding to the chemotherapeutic treatment. To account for the tumor shrinkage in the theoretical model, the boundary between tumor and normal liver tissue, $R_{TN}$, was placed at a radius of 2.3 mm. In the ablated model, drug transport from a centrally located implant in ablated tumor was simulated using an ablated tissue radius, $R_{AB}$, of 4.3 mm, corresponding to measurements in fresh tissue slices. The outer boundary of normal tissue, $R_{OB}$, was placed at 10 mm in both non-ablated and ablated models.

The drug distributions from the 1-D transport models in non-ablated and ablated tumor were then solved. With this model, previously estimated values for the diffusion coefficient ($D_{liver} = 6.7 \times 10^{-11}$ $m^2s^{-1}$) and elimination coefficient ($\gamma_{liver} = 9.6 \times 10^{-4}$ $s^{-1}$) were used for non-ablated, normal liver tissue surrounding the tumors [10]. The cylindrically symmetric model was spatially discretized with a uniform mesh spacing of 0.1 mm to match the spacing of the experimental data. This system was then solved using a finite element method (FEM) implemented by COMSOL 3.3 (Burlington, MA). The simulated model output consisted of the doxorubicin concentration as a function of radius at the experimentally measured times, 4 and 8 days. Values for *D* and $\gamma$ and their corresponding 95% confidence intervals in non-ablated and ablated tumor tissue were determined by least-squares fitting of the model simulated drug concentration distributions to the experimental data. This step was implemented using the *lsqcurvefit* function of MATLAB 7.1 (Mathworks, Natick, MA). Initially, *D* and $\gamma$ were assumed to be independent of position and time. When the model did not yield a good fit to the experimental data, however, these coefficients were represented as functions of *r* and/or *t* based on an understanding of the underlying physiology. Since various functional forms were consistent with changes in these coefficients, the final choices were those for which the model output most closely fit the data and involved the fewest number of model parameters.

### Three-dimensional (3-D) simulation method

To demonstrate that the estimated tissue parameters could be used more generally to determine drug concentrations throughout a tumor, treatment of tumors with a diameter of 2.0 cm was simulated in 3-D. This simulation phase considered two polymer millirods implant treatment strategies: (A) treatment of a non-ablated tumor (2.0 cm diam.) with a central implant; (B) treatment of a tumor (2.0 cm diam.) with ablation of 75% of the volume (1.8 cm diam.) and a central implant. Because these cases did not assume that transport was cylindrically symmetric, simulations were based on a 3-D drug transport model,

$$\frac{\partial C}{\partial t} = D\left(\frac{\partial^2 C}{\partial x^2} + \frac{\partial^2 C}{\partial y^2} + \frac{\partial^2 C}{\partial z^2}\right) - \gamma C \tag{6}$$

Boundary and initial conditions were set as described above with the exception that $R_{OB} = 4$ cm to allow for placement of larger tumors. Diffusion in the ablated region was scaled to the

larger size by setting the $R_{AB}$ at 0.9 cm and linearly scaling the spatial dependence of the diffusion parameter. Drug concentrations within the tumor were obtained using a 3-D FEM solution implemented by COMSOL. The two drug distributions were compared by calculating average drug concentrations in the entire tumor and an outer tumor region measuring 25% of the total tumor volume, which corresponds to the non-ablated region of geometry B. Therapies were further compared by determining the fractions of the tumor and risk volumes that were covered with greater than 2 times the known therapeutic value of doxorubicin in VX2 tumor, 6.4 μg/g [31,32].

## Results

### Drug transport in non-ablated tumors

Rates of drug diffusion and elimination in non-ablated tumors were estimated from drug distribution profiles measured 4 and 8 days after implant placement. Drug transport was approximated using transport coefficients that did not vary as a function of time or position. Experimental drug measurements compared to model generated output are shown in Figure 1. The estimated value of doxorubicin diffusion throughout non-ablated tumor, $D_{tumor}$, was calculated as $5.01 \pm 0.32 \times 10^{-11}$ $m^2 s^{-1}$. Doxorubicin elimination, $\gamma_{tumor}$, was calculated as $0.58 \pm 0.04 \times 10^{-4}$ $s^{-1}$.

### Drug transport in ablated tumors

Drug diffusion and elimination coefficients were estimated from ablated tumor drug distributions obtained 4 and 8 days after tumor ablation and implant placement. Using only constant parameters, the predicted concentration distribution did not yield a close fit to the experimental data; the model substantially overpredicted drug concentrations in the outer region of the ablated tumor on day 8. This finding suggested that constant model parameters were inadequate to simulate ablated tumor tissue. To more accurately predict drug transport in ablated tumors, diffusion and elimination coefficients that were a function of distance from the implant radius ($r$), time ($t$), or both were tested. Where possible, assumptions about the parameters were made based on *a priori* information, such as the physiology of ablation-induced damage and histological changes occurring after ablation, to minimize the number of parameters estimated.

Optimal model fits in ablated tumor (Figure 2) were obtained by using diffusion that varied as a function of $r$ and elimination that varied as a function of $t$. The diffusion rate of doxorubicin in ablated tissue was obtained by setting the diffusion rate in the center of the ablated tumor ($0.8 \leq r < 2.0$ mm) to a constant parameter, $D^{center}_{ablated\ tumor}$, and allowing the parameter to vary linearly between $D^{center}_{ablated\ tumor}$ and $D_{tumor}$ in the outer portion of the ablated tumor ($2.0 \leq r < 4.3$ mm),

$$D = \begin{cases} r < 2\,\text{mm} : D^{center}_{ablated\ tumor} \\ r \geq 2\,\text{mm} : D^{center}_{ablated\ tumor} - \left(\frac{r - 2\,\text{mm}}{4.3 - 2\,\text{mm}}\right)\left(D^{center}_{ablated\ tumor} - D_{tumor}\right) \end{cases} \quad (7)$$

In this equation, 2 mm was chosen as the distance for the change in the diffusion parameter function by testing several different locations and determining which model output most closely approximated the experimental data. Additionally, 4.3 mm was chosen as the outer boundary of the ablated region because this was the experimentally measured size of the ablation coagulated region. The piecewise linear function of $D$ was constant for the 8 day period of the study. In contrast, the elimination coefficient gave the best model fit when it varied as a function of $t$ and not $r$. The elimination coefficient was set to a constant value of 0 for the

first four days of the study, after which it was allowed to vary linearly between 0 and elimination on day 8, $\gamma_{ablated\ tumor}^{day\ 8}$,

$$\gamma = \begin{Bmatrix} t < 4\ \text{days} : 0 \\ t \geq 4\ \text{days} : \left(\frac{t - 4\ \text{days}}{4\ \text{days}}\right)\gamma_{ablated\ tumor}^{day\ 8} \end{Bmatrix} \quad (8)$$

This pattern of elimination was chosen based on the mechanism of tissue destruction due to RF ablation. Previous modeling work has shown that after ablation of normal tissue, the elimination rate is reduced to zero, a reasonable finding because ablation destroys the living tissue and stops blood flow to the area. However, because ablation also induces a wound healing response that includes the formation of new blood vessels in the injured region, the elimination may begin to return several days after ablation. In this case, 4 days was chosen as the inflection point because experimental data and previously published reports indicated that this was about the time when new blood vessels would begin forming after tissue injury [33]. Using this parameter structure, which is shown in Figure 3, $D_{ablated\ tumor}^{center}$ was estimated to be 8.76 ± $0.41 \times 10^{-11}\ m^2 s^{-1}$, and $\gamma_{ablated\ tumor}^{day\ 8}$ was determined to be $0.57 \pm 0.04 \times 10^{-4}\ s^{-1}$. Parameter structures with greater parameter complexity, such as power and exponential growth, did not improve the quality of the model fits. Furthermore, functions that allowed each parameter to vary simultaneously as a function of *t* and *r* increased the number of parameters required and did not improve the model approximation.

## Histology of ablated tumors

Histology of tumor tissues treated with RF ablation followed by polymer implants provided physiological insights on the pattern of tissue destruction for comparison with quantitative transport information. H&E stained sections at the center and periphery of the ablated region on day 8 indicated some essential differences between tissues in these regions (Figure 4). Tissue approximately 1–2 mm from the ablation probe tip showed extensive necrosis and protein denaturation, with few visible nuclei or intact cell membranes. Damage to this region was extensive and indicative of high heat exposure. At a distance of 3–4 mm from the ablation probe, a different structural pattern was seen. Cells showed pallor, pyknotic nuclei, and shrunken cytoplasm while retaining much of their underlying morphology. This finding was consistent with tissues receiving a lower heat dose but loss of blood supply. This pattern substantiated the choice of a diffusion parameter which varied with radius in the model. The structure of tissue in the center of the ablated region was more extensively destroyed, and this region corresponded to the location of ablated tissue which had a higher estimated diffusion rate in the model. Tumor around the periphery that was exposed to less heat was less severely damaged, and exhibited a diffusion rate that deviated less from normal tissue.

Comparative histology between 4 and 8 days also revealed time-dependent processes that took place in the ablated tissue (Figure 5). Ablated tumor after 4 days showed significant signs of coagulative necrosis, featuring numerous blood vessels filled with coagulated red blood cells, particularly around the ablation periphery. Lack of patent blood vessels in the day 4 tissue was compatible with the initial segment of the elimination function, which had a value of zero. However, by day 8 the region revealed progression of the ablation-induced injury. In addition to granulation tissue found around the boundary, moderate amounts of new blood vessels were seen throughout the ablated region. This day 8 tissue section provided evidence supporting the assumption that elimination returns gradually between 4 and 8 days after ablation.

### Three-dimensional (3-D) simulation of tumor transport

With the diffusion and elimination coefficients determined from the 1-D model analysis, a 3-D model was applied to simulate treatment scenarios for a larger tumor. Drug distribution was simulated from 0 to 8 days after a doxorubicin millirod was centrally placed in a 2.0 cm diameter tumor: (A) without thermal ablation (B) following RF ablation of 75% of the tumor volume (1.8 cm diameter). A sample finite element mesh and corresponding results for the two scenarios are shown in Figure 6. Over 8 days, the average drug concentrations in the entire tumor were 32 and 119 μg/g in the non-ablated and ablated case, respectively. When considering the outer rim of tumor within 1 mm of normal liver, average concentrations dropped to 0.2 μg/g in the non-ablated scenario or 17 μg/g in the ablated scenario. None of the tissue in the outer rim reached the therapeutic margin (13 μg/g, or 2x the known therapeutic value) without ablation, but ablation pretreatment increased coverage of the outer tumor to 80% of the outer rim volume. Finally, total drug released from the simulated implants in ablated tumor was 2.6 mg compared with 3.6 mg in non-ablated tumor.

## Discussion

In this study, mass transport modeling was used to estimate doxorubicin transport in tumor tissues and then to simulate drug distribution in a larger tumor. In addition to providing doxorubicin transport parameters, this work represents an improvement in methodology that can be used in future work. The finite element method (FEM) of solving the model provided a flexible platform that had advantages over an analytical solution, such as the ability to use arbitrary geometries or functions that are not easily expressed analytically [34–37]. This flexibility allowed transport modeling with space and time variant parameters, representing a significant advancement in modeling drug transport in ablated tissues that had not been accomplished previously. Additionally, future uses of this model can simulate drug transport in scenarios that are not symmetric or incorporate spatial data about a tumor into the model.

### Estimation of doxorubicin transport properties in tumors

Simulation of drug transport using the model allowed for reasonable approximation of drug release from doxorubicin millirods placed in tumors. In Table 1, estimated values of tissue transport parameters are summarized along with previous values from Qian et al. in which parameters were calculated from drug distribution data measured from 1 hour to 4 days [10]. The estimated value for diffusion in non-ablated liver tumors was 25% lower than diffusion in non-ablated normal liver tissue. This may have occurred because tumors are often comprised of dense tissue with high cellularity, elevated collagen content, and a tortuous extracellular matrix, all of which can act as a barrier to drug transport [38,39]. The elimination rate in tumor was 6% of the value in normal liver, indicating that doxorubicin was removed from tumor at a drastically lower rate. Normal liver parenchyma is heavily populated with blood vessels and sinusoids, and hepatocytes may have high enzymatic activity for drug elimination. Additionally, the VX2 tumors used in this study may have a lower blood vessel density and may metabolize drug more slowly than normal liver.

### Ablation-induced changes in tumor doxorubicin transport

In the ablated tumor tissue, diffusion was best represented by a function of radius, while elimination was best represented by a function of time. After ablation, diffusion at the center of the tumor region was increased by 75% over non-ablated tumor. This finding is in contrast to the previous results showing that ablation decreased the diffusion coefficient in normal liver [10]. However, several other studies have demonstrated that drug diffusion rates could be increased by using an apoptosis-inducing drug pretreatment to reduce barriers to drug transit [28,29]. Analogously, RF ablation may increase the rate of doxorubicin diffusion by disrupting tumor morphology and cellular structure. Changes in the diffusion value did not extend to the

ablation periphery, which had the same diffusion value as non-ablated tumor. This finding suggests that RF-induced structural damage to the tumor may not be uniform throughout the tumor, with higher damage found at the center of the coagulated region. The temperature distribution during ablation, with high temperatures near the ablation probe that gradually decrease to normal at the ablation periphery [40], can explain this fundamental difference. Moreover, these values may vary little with time because the initial ablation tissue damage resolves very slowly over time. Histology corroborated the pattern of more extensive cell damage at the center of the ablation region. Other published reports of tumor ablation support the finding that RF-induced damage is not homogeneous throughout the ablated region [41, 42].

In contrast, elimination could be represented as a homogenous function throughout the ablated region that varied as a function of time. RF ablation reduced tumor drug elimination to zero for the first four days after treatment, consistent with previous results in ablated liver tissue [10]. This finding is likely because the heat exposure to the entire ablated region was sufficient to coagulate all of the blood vessels. However, elimination in the ablated tumor increased as a function of time between days 4 and 8, which was not observed in the previous study that stopped at day 4. This increase in elimination between days 4 and 8 could result from the host inflammatory response to the ablation. Histology of the ablated tumors demonstrated the infiltration of inflammatory cells and formation of new blood vessels, which could explain the return of elimination as a function of time. A few small blood vessels exerted a sizeable effect on drug elimination without affecting diffusion because they comprised a small fraction of the total ablated volume. Overall, choosing the diffusion rate coefficient as a function of position and elimination coefficient as a function of time allowed for effective simulation of drug distribution in ablated tumors.

## Simulation of drug distribution in larger tumors

Three-dimensional simulation of a larger, more clinically relevant tumor treated locally with a doxorubicin-containing implant without or following RF thermal ablation demonstrated the ability to evaluate 3-D scenarios based on their expected drug distributions. First, the feasibility of using parameters from a 1-D model simulation for application in a 3-D simulation of a larger tumor was established. Because it was solved using a finite element method, this 3-D simulation strategy could be implemented in situations that are not symmetric, such as when multiple implants are placed around the periphery of a tumor. Second, the simulation reaffirmed previous findings about using ablation before implant placement. Ablation drastically decreased drug elimination in the tumor region, which had the most pronounced effects on drug retention in the peripheral tumor region. While experimentally observed previously, this effect appeared to be more substantial in the larger simulated tumors. Furthermore, RF ablation allowed for significantly slower drug release from the implant, depleting the implant more slowly and maintaining a therapeutic level, especially at the tumor periphery, for a longer period. These simulations provide the basis for designing future animal experiments to confirm these conclusions and validate the extension of this model into a larger tumor. Additionally, the model could be used in the future to anticipate how other changes to implant design, such as modifying the drug release rate or including dexamethasone to moderate the inflammatory response after ablation [43], could affect drug distribution in the tumors. This computational strategy should allow for rapid development and prototyping of different implant designs that can optimally treat larger, more clinically relevant tumor models. Ultimately, this drug transport model may be used as part of a comprehensive treatment planning tool. After acquiring imaging data about tumor geometry, ablation treatment could be planned using a thermal damage model, and drug coverage in the ablated tumor could be predicted using this 3-D finite element model.

## Conclusion

This computational model provided a feasible means of estimating drug distribution dynamics following placement of an intratumoral chemotherapeutic implant. RF ablation was shown to facilitate intratumoral drug delivery in tissue not only by reducing normal elimination processes but also by increasing diffusion. Extension of parameter estimates from a 1-D model into a 3-D simulation further demonstrated the benefits of ablation in conjunction with drug delivery. The computational modeling approach indicates the advantages of using simulation to design and rapidly prototype new implant treatment strategies.

#### Acknowledgements

This work was supported by NIH grant R01 CA90696 to JG. BW and RP are supported in part by the NIH grant T32 GM07250 to the Case Western Reserve University Medical Scientist Training Program. BW is also supported by DOD predoctoral fellowship BC043453. This is manuscript CSCN 016 from the 'Cell Stress and Cancer Nanomedicine' program in the Simmons Comprehensive Cancer Center at the University of Texas Southwestern Medical Center at Dallas.

## References

1. Pacella CM, Valle D, Bizzarri G, Pacella S, Brunetti M, Maritati R, Osborn J, Stasi R. Percutaneous laser ablation in patients with isolated unresectable liver metastases from colorectal cancer: Results of a phase II study. Acta Oncol 2006;45(1):77–83. [PubMed: 16464799]
2. Simon CJ, Dupuy DE, Iannitti DA, Lu DS, Yu NC, Aswad BI, Busuttil RW, Lassman C. Intraoperative triple antenna hepatic microwave ablation. AJR Am J Roentgenol 2006;187(4):W333–340. [PubMed: 16985103]
3. Amersi FF, McElrath-Garza A, Ahmad A, Zogakis T, Allegra DP, Krasne R, Bilchik AJ. Long-term survival after radiofrequency ablation of complex unresectable liver tumors. Arch Surg 2006;141(6): 581–587. [PubMed: 16785359]discussion 587–588
4. Tateishi R, Shiina S, Teratani T, Obi S, Sato S, Koike Y, Fujishima T, Yoshida H, Kawabe T, Omata M. Percutaneous radiofrequency ablation for hepatocellular carcinoma. An analysis of 1000 cases. Cancer 2005;103(6):1201–1209. [PubMed: 15690326]
5. Clark HP, Carson WF, Kavanagh PV, Ho CP, Shen P, Zagoria RJ. Staging and current treatment of hepatocellular carcinoma. Radiographics 2005;25(Suppl 1):S3–23. [PubMed: 16227495]
6. Harrison LE, Koneru B, Baramipour P, Fisher A, Barone A, Wilson D, Dela Torre A, Cho KC, Contractor D, Korogodsky M. Locoregional recurrences are frequent after radiofrequency ablation for hepatocellular carcinoma. J Am Coll Surg 2003;197(5):759–764. [PubMed: 14585410]
7. Yu HC, Cheng JS, Lai KH, Lin CP, Lo GH, Lin CK, Hsu PI, Chan HH, Lo CC, Tsai WL, Chen WC. Factors for early tumor recurrence of single small hepatocellular carcinoma after percutaneous radiofrequency ablation therapy. World J Gastroenterol 2005;11(10):1439–1444. [PubMed: 15770718]
8. Gao J, Qian F, Szymanski-Exner A, Stowe N, Haaga J. In vivo drug distribution dynamics in thermoablated and normal rabbit livers from biodegradable polymers. J Biomed Mater Res 2002;62 (2):308–314. [PubMed: 12209952]
9. Qian F, Saidel GM, Sutton DM, Exner A, Gao J. Combined modeling and experimental approach for the development of dual-release polymer millirods. J Control Release 2002;83(3):427–435. [PubMed: 12387950]
10. Qian F, Stowe N, Liu EH, Saidel GM, Gao J. Quantification of in vivo doxorubicin transport from PLGA millirods in thermoablated rat livers. J Control Release 2003;91(1–2):157–166. [PubMed: 12932647]
11. Qian F, Stowe N, Saidel GM, Gao J. Comparison of doxorubicin concentration profiles in radiofrequency-ablated rat livers from sustained- and dual-release PLGA millirods. Pharm Res 2004;21(3):394–399. [PubMed: 15070087]
12. Szymanski-Exner A, Gallacher A, Stowe NT, Weinberg B, Haaga JR, Gao J. Local carboplatin delivery and tissue distribution in livers after radiofrequency ablation. J Biomed Mat Res 2003;67A (2):510–516.

13. Weinberg BD, Ai H, Blanco E, Anderson JM, Gao J. Antitumor efficacy and local distribution of doxorubicin via intratumoral delivery from polymer millirods. J Biomed Mater Res A 2007;81(1): 161–170. [PubMed: 17120197]
14. Weinberg BD, Blanco E, Lempka SF, Anderson JM, Exner AA, Gao J. Combined radiofrequency ablation and doxorubicin-eluting polymer implants for liver cancer treatment. J Biomed Mater Res A 2007;81(1):205–213. [PubMed: 17120205]
15. Qian F, Nasongkla N, Gao J. Membrane-encased polymer millirods for sustained release of 5-fluorouracil. J Biomed Mater Res 2002;61(2):203–211. [PubMed: 12007200]
16. Au JL, Jang SH, Zheng J, Chen CT, Song S, Hu L, Wientjes MG. Determinants of drug delivery and transport to solid tumors. J Control Release 2001;74(1–3):31–46. [PubMed: 11489481]
17. Banerjee RK, van Osdol WW, Bungay PM, Sung C, Dedrick RL. Finite element model of antibody penetration in a prevascular tumor nodule embedded in normal tissue. J Control Release 2001;74(1–3):193–202. [PubMed: 11489495]
18. Guse C, Koennings S, Kreye F, Siepmann F, Goepferich A, Siepmann J. Drug release from lipid-based implants: elucidation of the underlying mass transport mechanisms. Int J Pharm 2006;314(2): 137–144. [PubMed: 16503388]
19. Siepmann J, Siepmann F, Florence AT. Local controlled drug delivery to the brain: mathematical modeling of the underlying mass transport mechanisms. Int J Pharm 2006;314(2):101–119. [PubMed: 16647231]
20. Shah SA, Cleary SP, Wei AC, Yang I, Taylor BR, Hemming AW, Langer B, Grant DR, Greig PD, Gallinger S. Recurrence after liver resection for hepatocellular carcinoma: risk factors, treatment and outcomes. Surgery 2007;141(3):330–339. [PubMed: 17349844]
21. Strasser JF, Fung LK, Eller S, Grossman SA, Saltzman WM. Distribution of 1,3-bis(2-chloroethyl)-1-nitrosourea and tracers in the rabbit brain after interstitial delivery by biodegradable polymer implants. J Pharmacol Exp Ther 1995;275(3):1647–1655. [PubMed: 8531140]
22. Wang CC, Li J, Teo CS, Lee T. The delivery of BCNU to brain tumors. J Control Release 1999;61 (1–2):21–41. [PubMed: 10469900]
23. Tao A, Tao L, Nicholson C. Cell cavities increase tortuosity in brain extracellular space. J Theor Biol 2005;234(4):525–536. [PubMed: 15808873]
24. Tan WH, Wang F, Lee T, Wang CH. Computer simulation of the delivery of etanidazole to brain tumor from PLGA wafers: comparison between linear and double burst release systems. Biotechnol Bioeng 2003;82(3):278–288. [PubMed: 12599254]
25. Kalyanasundaram S, Calhoun VD, Leong KW. A finite element model for predicting the distribution of drugs delivered intracranially to the brain. Am J Physiol 1997;273(5 Pt 2):R1810–1821. [PubMed: 9374827]
26. Neeves KB, Lo CT, Foley CP, Saltzman WM, Olbricht WL. Fabrication and characterization of microfluidic probes for convection enhanced drug delivery. J Control Release 2006;111(3):252–262. [PubMed: 16476500]
27. Raghavan R, Brady ML, Rodriguez-Ponce MI, Hartlep A, Pedain C, Sampson JH. Convection-enhanced delivery of therapeutics for brain disease, and its optimization. Neurosurg Focus 2006;20 (4):E12. [PubMed: 16709017]
28. Au JL, Jang SH, Wientjes MG. Clinical aspects of drug delivery to tumors. J Control Release 2002;78 (1–3):81–95. [PubMed: 11772451]
29. Lu D, Wientjes MG, Lu Z, Au JL. Tumor priming enhances delivery and efficacy of nanomedicines. J Pharmacol Exp Ther 2007;322(1):80–88. [PubMed: 17420296]
30. Qian F, Szymanski A, Gao JM. Fabrication and characterization of controlled release poly(D,L-lactide-co-glycolide) millirods. Journal of Biomedical Materials Research 2001;55(4):512–522. [PubMed: 11288079]
31. Ridge JA, Collin C, Bading JR, Hancock C, Conti PS, Daly JM, Raaf JH. Increased adriamycin levels in hepatic implants of rabbit Vx-2 carcinoma from regional infusion. Cancer Res 1988;48(16):4584–4587. [PubMed: 3396009]
32. Swistel AJ, Bading JR, Raaf JH. Intraarterial versus intravenous adriamycin in the rabbit Vx-2 tumor system. Cancer 1984;53(6):1397–1404. [PubMed: 6692329]

33. Anderson JM. Mechanisms of inflammation and infection with implanted devices. Cardiovascular Pathology 1993;2(3 Supplement 1):33–41.
34. Frenning G, Brohede U, Stromme M. Finite element analysis of the release of slowly dissolving drugs from cylindrical matrix systems. J Control Release 2005;107(2):320–329. [PubMed: 16081182]
35. Haddish-Berhane N, Nyquist C, Haghighi K, Corvalan C, Keshavarzian A, Campanella O, Rickus J, Farhadi A. A multi-scale stochastic drug release model for polymer-coated targeted drug delivery systems. J Control Release 2006;110(2):314–322. [PubMed: 16288814]
36. Huang J, Wong HL, Zhou Y, Wu XY, Grad H, Komorowski R, Friedman S. In vitro studies and modeling of a controlled-release device for root canal therapy. J Control Release 2000;67(2–3):293–307. [PubMed: 10825562]
37. Tzafriri AR. Mathematical modeling of diffusion-mediated release from bulk degrading matrices. J Control Release 2000;63(1–2):69–79. [PubMed: 10640581]
38. Netti PA, Berk DA, Swartz MA, Grodzinsky AJ, Jain RK. Role of extracellular matrix assembly in interstitial transport in solid tumors. Cancer Res 2000;60(9):2497–2503. [PubMed: 10811131]
39. McGuire S, Zaharoff D, Yuan F. Nonlinear dependence of hydraulic conductivity on tissue deformation during intratumoral infusion. Ann Biomed Eng 2006;34(7):1173–1181. [PubMed: 16791492]
40. Johnson PC, Saidel GM. Thermal model for fast simulation during magnetic resonance imaging guidance of radio frequency tumor ablation. Ann Biomed Eng 2002;30(9):1152–1161. [PubMed: 12502226]
41. Coad JE, Kosari K, Humar A, Sielaff TD. Radiofrequency ablation causes ‘thermal fixation’ of hepatocellular carcinoma: a post-liver transplant histopathologic study. Clin Transplant 2003;17(4):377–384. [PubMed: 12868996]
42. Nikfarjam M, Muralidharan V, Christophi C. Mechanisms of focal heat destruction of liver tumors. J Surg Res 2005;127(2):208–223. [PubMed: 16083756]
43. Blanco E, Weinberg BD, Stowe NT, Anderson JM, Gao J. Local release of dexamethasone from polymer millirods effectively prevents fibrosis after radiofrequency ablation. J Biomed Mater Res A 2006;76(1):174–182. [PubMed: 16265662]

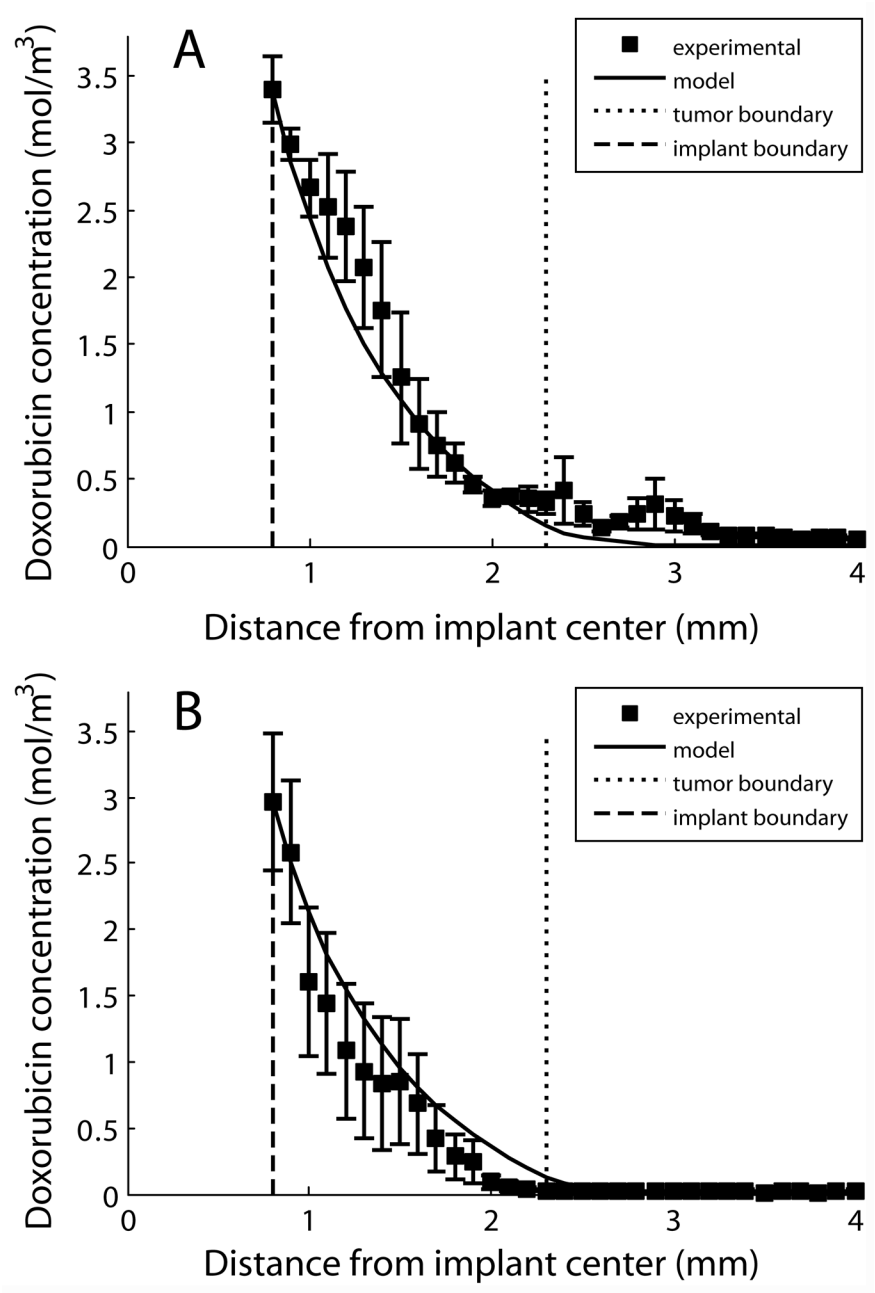


**Figure 1.**
Modeling results from parameter estimation in non-ablated tumor. Experimental radial drug distributions are shown compared to model output on day 4 (A, n = 3) and day 8 (B, n = 4). The error bars show the standard error of the mean.

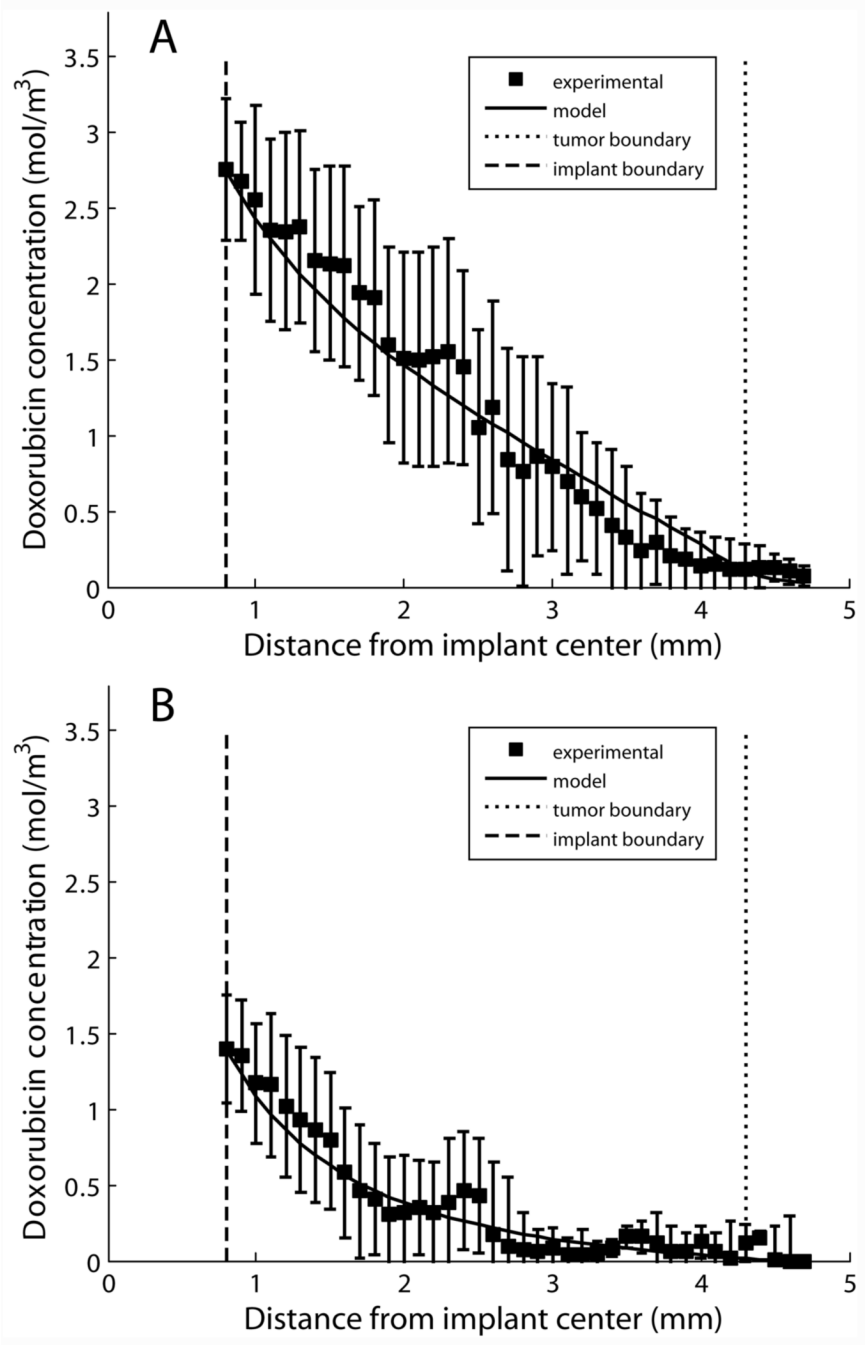


**Figure 2.**
Modeling results from parameter estimation in ablated tumor. Experimental radial drug distributions are shown compared to model output on day 4 (A, n = 4) and day 8 (B, n = 3). The error bars show the standard error of the mean.

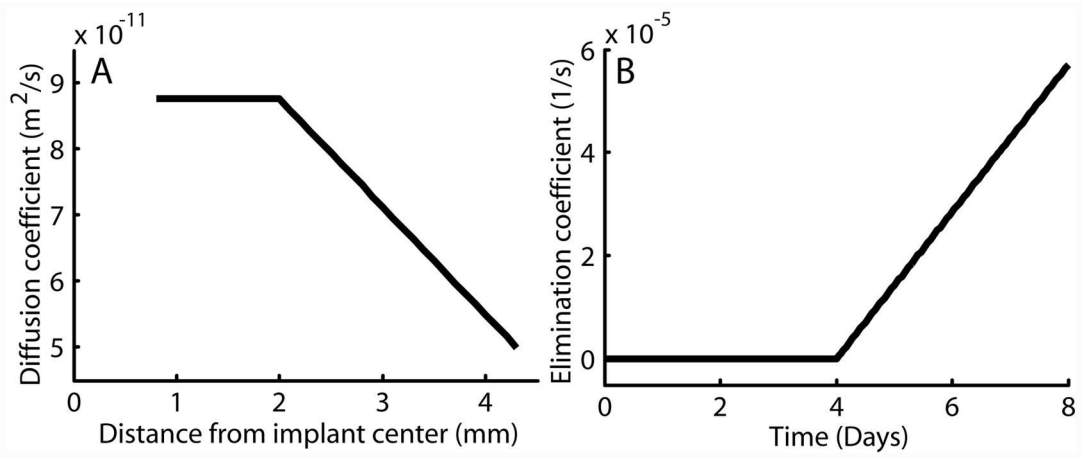


**Figure 3.**
Graphs showing radial dependence of the diffusion coefficient, *D* (A), and time dependence of the elimination coefficient, $\gamma$ (B), in ablated tumor.

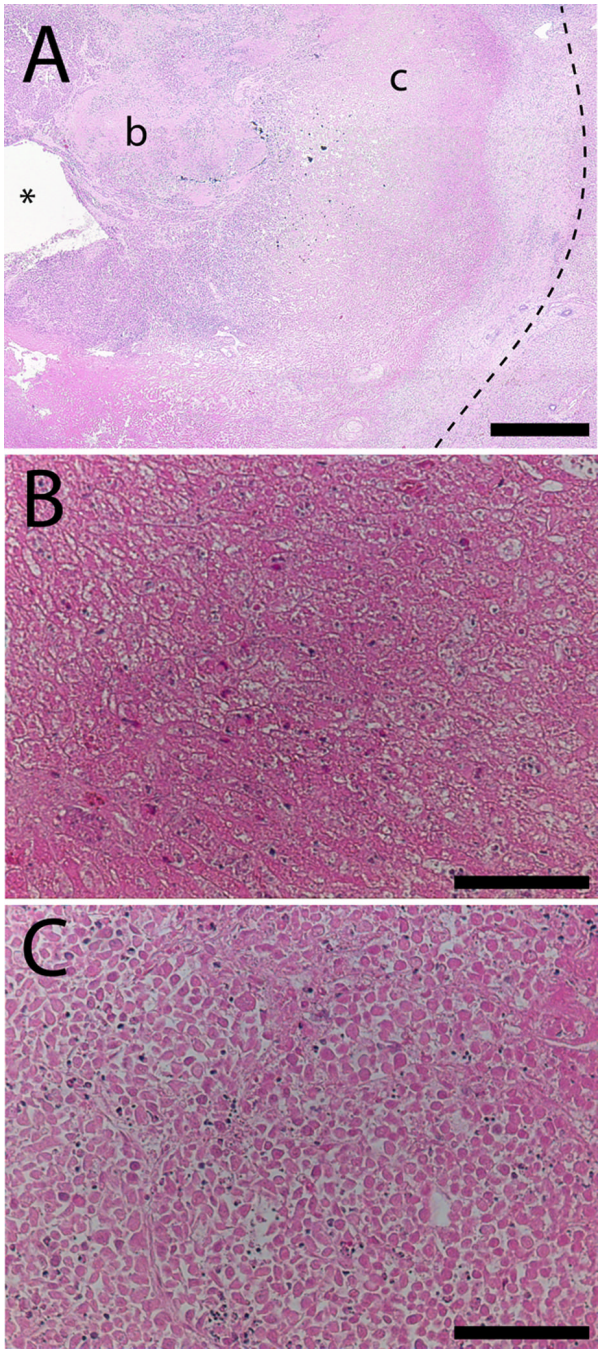


**Figure 4.**
H&E stained overview slide of ablated tumor tissue (A) showing the relative location of the high magnification regions (b, c) with respect to the ablation probe (*). The outer ablation boundary is indicated by a dashed line. Tissue near the probe (B) has lost its cellular structure and cell membranes, while tissue 4 mm from the probe (C) contains dead cells with no nuclei but overall structure largely intact. Scale bars are 1 mm (A) and 100 μm (B, C).

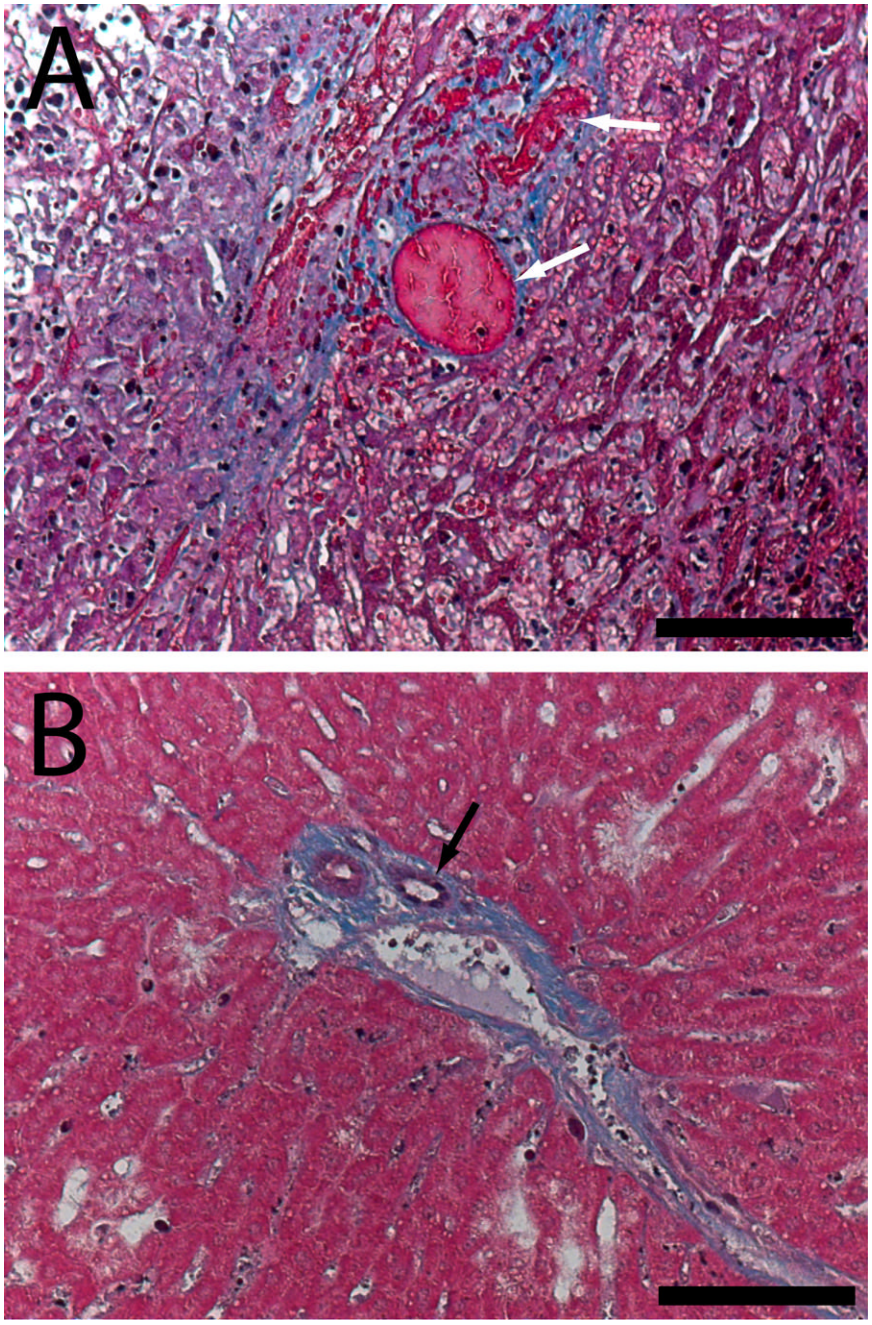


**Figure 5.**
Masson's trichrome histology showing coagulated blood vessels (white arrows) in the ablated tumor region 4 days after ablation (A). By day 8 (B), new blood vessels (black arrow) are forming in the ablated region. Scale bars are 100 μm.

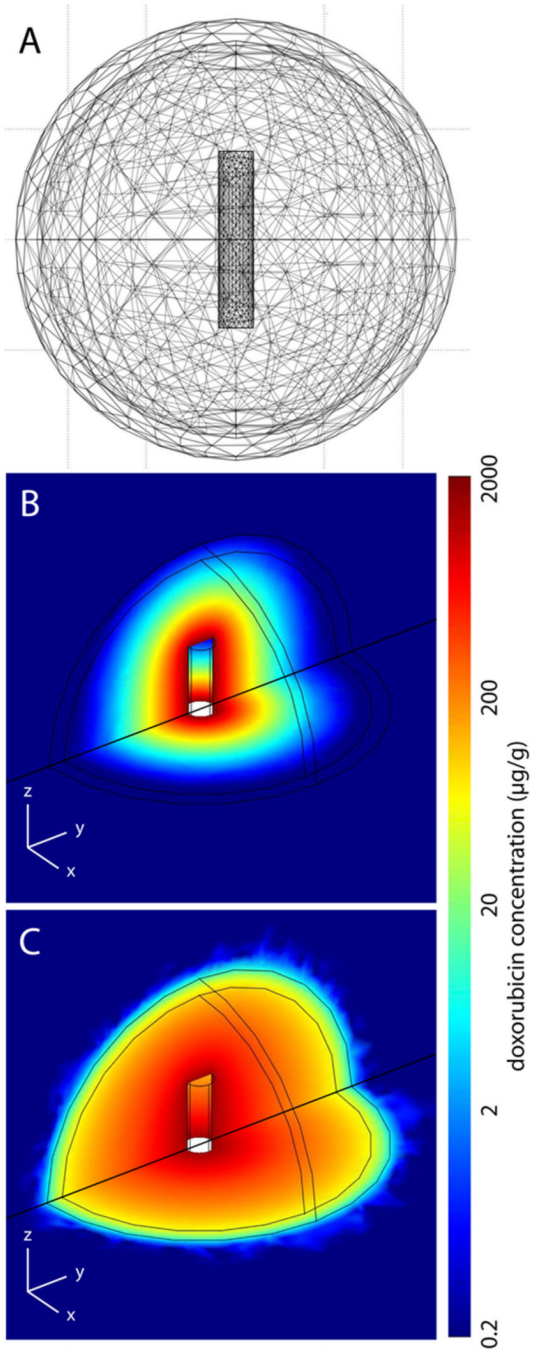


**Figure 6.**
3-D modeling of drug distributions in a 2.0 cm tumor. Finite element mesh used to simulate the drug transport (A) along with simulated drug distributions 4 days after implant placement in a non-ablated (B) and ablated (C) tumor.

**Table 1**

Summary of doxorubicin transport parameters in liver and liver tumor.

| | | Diffusion ($m^2/s$, $\times 10^{-11}$) | Elimination (1/s, $\times 10^{-4}$) |
|---|---|---|---|
| **Liver*** | **Non-ablated** | 6.7 | 9.6 |
| | **Ablated** | 1.1 | 0 |
| **Tumor** | **Non-ablated** | 5.01 ± 0.32 | 0.58 ± 0.04 |
| | **Ablated** | 8.76 ± 0.41 *(center)*<br>5.01 ± 0.32 *(periphery)* | 0 *(days 0–4)*<br>0.57 ± 0.03 *(day 8)* |

Values are shown ± 95% confidence interval.

* indicates that the values were taken from Qian, et al. [10]